

A Journal of the Gesellschaft Deutscher Chemiker

Angewandte Chemie

GDCh

International Edition

www.angewandte.org

Accepted Article

Title: Dual Metallosalen-based Covalent Organic Frameworks for Artificial Photosynthetic Diluted CO₂ Reduction

Authors: Hong Dong, Liang Fang, Ke-Xin Chen, Jian-Xin Wei, Jia-Xin Li, Xiu Qiao, Ya Wang, Feng-Ming Zhang, and Ya-Qian Lan

This manuscript has been accepted after peer review and appears as an Accepted Article online prior to editing, proofing, and formal publication of the final Version of Record (VoR). The VoR will be published online in Early View as soon as possible and may be different to this Accepted Article as a result of editing. Readers should obtain the VoR from the journal website shown below when it is published to ensure accuracy of information. The authors are responsible for the content of this Accepted Article.

To be cited as: *Angew. Chem. Int. Ed.* **2024**, e202414287

Link to VoR: <https://doi.org/10.1002/anie.202414287>

RESEARCH ARTICLE

Dual Metallosalen-based Covalent Organic Frameworks for Artificial Photosynthetic Diluted CO₂ ReductionHong Dong,^{*,[a]} Liang Fang,^{*,[a]} Ke-Xin Chen,^[a] Jian-Xin Wei,^[a] Jia-Xin Li,^[a] Xiu Qiao,^[a] Ya Wang,^[a] Feng-Ming Zhang^{*,[a]} and Ya-Qian Lan^{*,[b]}

Dedication ((optional))

[a] Dr. H. Dong, L. Fang, K.-X. Chen, J.-X. Wei, J.-X. Li, X. Qiao, Y. Wang, Prof. F.-M. Zhang

Heilongjiang Provincial Key Laboratory of CO₂ Resource Utilization and Energy Catalytic Materials, School of Material Science and Chemical Engineering
Harbin University of Science and Technology

Harbin 150040, PR China

E-mail: zhangfm80@163.com

[b] Prof. Y.-Q. Lan

School of Chemistry

South China Normal University

Guangzhou 510006, PR China

E-mail: yqlan@m.scnu.edu.cn

[*] These authors contributed equally to this work.

Supporting information for this article is given via a link at the end of the document.

Abstract: Directly converting CO₂ in flue gas using artificial photosynthetic technology represents a promising green approach for CO₂ resource utilization. However, it remains a great challenge to achieve efficient reduction of CO₂ from flue gas due to the decreased activity of photocatalysts in diluted CO₂ atmosphere. Herein, we designed and synthesized a series of dual metallosalen-based covalent organic frameworks (MM-Salen-COFs, M: Zn, Ni, Cu) for artificial photosynthetic diluted CO₂ reduction and confirmed their advantage in comparison to that of single metal M-Salen-COFs. As a results, the ZnZn-Salen-COF with dual Zn sites exhibits a prominent visible-light-driven CO₂-to-CO conversion rate of 150.9 μmol g⁻¹ h⁻¹ under pure CO₂ atmosphere, which is ~6 times higher than that of single metal Zn-Salen-COF. Notably, the dual metal ZnZn-Salen-COF still displays efficient CO₂ conversion activity of 102.1 μmol g⁻¹ h⁻¹ under diluted CO₂ atmosphere from simulated flue gas conditions (15% CO₂), which is a record high activity among COFs- and MOFs-based photocatalysts under the same reaction conditions. Further investigations and theoretical calculations suggest that the synergistic effect between the neighboring dual metal sites in the ZnZn-Salen-COF facilitates low concentration CO₂ adsorption and activation, thereby lowering the energy barrier of the rate-determining step.

Introduction

Artificial photosynthetic CO₂ reduction with the aim of converting CO₂ into fuels or valuable chemicals, holds great importance in addressing mitigate global warming and advancing sustainability efforts by reducing greenhouse gas emissions.^[1] Over the past few decades, researchers have made significant progress in developing semiconductor-based artificial photocatalysts for efficiently converting CO₂ into desired products.^[2] Until now, the reported CO₂ reduction activity of artificial photosynthetic catalysts has been enhanced significantly

and more reduced chemical products were known.^[3] However, most studies and evaluations of photocatalysts mainly focused on the reduction of high concentration CO₂, and efforts to reduce low concentration CO₂ often resulted in lower photocatalytic activity.^[4] Given that CO₂ concentration in flue gases is relatively low (10–15%), it is crucial to develop robust catalysts that can effectively convert diluted CO₂ into high value-added products. Moreover, direct artificial photosynthetic conversion of CO₂ from flue gas can avoid the high energy consumption process of CO₂ enrichment, which is regarded as a green and low-cost way realizing the practical utilization of CO₂ from flue gas in the future.

Crystalline and porous materials, such as metal–organic frameworks (MOFs) and covalent organic frameworks (COFs), are emerging as advanced photocatalysts due to their high surface area, tunable pore size and tailorable band structures.^[5] In contrast to MOFs, the COFs are assembled through covalent bond connections of organic building blocks, typically exhibiting large conjugated systems, layered structures, and excellent visible-light-harvesting capabilities as photocatalysts.^[6] Metal covalent organic frameworks (M-COFs), assembled by anchoring metal ions onto the backbone of COFs, integrate the photocatalytic advantages of 2D COFs and abundant metal sites merits of MOFs. As a result, M-COFs are regarded as promising catalysts for photocatalytic CO₂ reduction reaction (CO₂RR).^[7] Additionally, the M-COFs represent a convergence of organometallic and polymer chemistry, which could significantly contribute to the development of high-quality heterogeneous catalysts with well-dispersed single metal sites.^[8] Within M-COFs, the type of single metal site and the coordination microenvironments can be readily tuned to facilitate the adsorption and activation of CO₂ molecules.^[9] Examples include metalloporphyrins or metal phthalocyanines based COFs,^[10] metallosalen-based COFs,^[11] and other M-COFs with post-coordinated single metal site.^[12] However, differently from the

RESEARCH ARTICLE

reduction of pure CO₂, the photocatalytic activities of these reported single-metal-site M-COFs in diluted CO₂ reduction are still relatively low. Generally, the CO₂ absorbing ability of metal ions as active sites in CO₂RR are moderate compared to Mg²⁺ and alkali metal cations ions with high absorbing energy to CO₂ molecules.^[13] Thus, the slow absorbing kinetics of single-metal-site photocatalysts towards CO₂ molecules in diluted atmosphere impede the whole catalytic reaction efficiency.^[14]

Recent works have shown that dual metal sites dispersed photocatalysts often exhibit greater potential in enhanced photocatalytic CO₂ reduction activity due to the synergistic adsorption and activation to CO₂ molecules and stabilizing key intermediates of CO₂RR from dual metal sites.^[15] For examples, the improved photocatalytic CO₂RR activity of binuclear Co ions anchored on lipid bilayer has recently been confirmed due to the synergistic adsorption and activation of the neighbouring Co ions to CO₂ molecules, which significantly reduced the reaction barriers for the formation of COOH* and the desorption of CO.^[16] The construction and regulation of dual metal sites catalysts also have been widely used in improved electrocatalytic CO₂ reduction. Thus, we reasoned that dual metal photocatalysts probably possess intrinsic potential in diluted CO₂ reduction by utilizing the advantage of dual metal sites in absorbing and converting CO₂ molecules. Unfortunately, although various structures of M-COFs have been reported, dual metal M-COFs photocatalysts are still very rare until now, and the attempt with dual metal M-COFs for

diluted CO₂ reduction is still a blank. In fact, it is a feasible way of designing dual metal COFs by constructing the structural model of available planar dual nuclear metal complexes in M-COFs skeleton, which is a rational way of designing the aimed M-COFs at molecular level.

In this work, we transfer the structural model of planar dual metal Salen complex into M-COFs, to construct a series of dual metal sites dispersed Salen-based COFs (MM-Salen-COFs, M: Zn, Ni, Cu) by acid-catalyzed Schiff base reaction and *in situ* coordination of metal ions for artificial photosynthetic CO₂ reduction. In this system, the ZnZn-Salen-COF with dual Zn sites exhibits the highest visible-light-driven CO₂-to-CO conversion activity of 150.9 μmol g⁻¹ h⁻¹, which is ~6 times higher than the single metal Zn-Salen-COF. Notably, the dual-metal ZnZn-Salen-COF still displays a remarkable CO₂ conversion activity of 102.1 μmol g⁻¹ h⁻¹ under a diluted CO₂ atmosphere from simulated flue gas (15% CO₂), which is a record high activity among COF- and MOF-based photocatalysts for diluted CO₂ reduction under the same reaction conditions. Further investigations and theoretical calculations suggest that the synergistic effect between the neighboring dual metal sites in the ZnZn-Salen-COF facilitates low concentration CO₂ adsorption and activation, thereby lowering the energy barrier of the rate-determining step. This work provides a new strategy of constructing synergistic dual metal sites in M-COFs for artificial photosynthetic diluted CO₂ reduction.

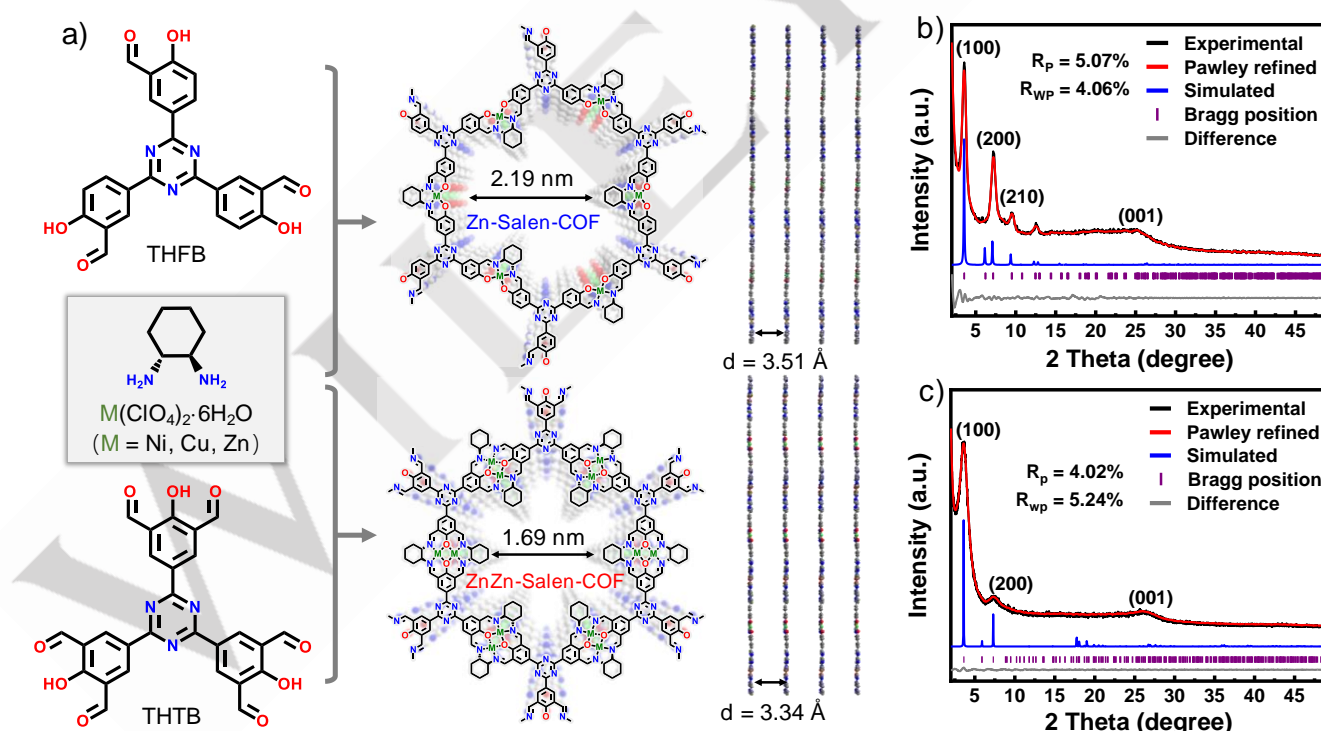


Figure 1. a) Synthetic scheme for the preparation and the structures of Zn-Salen-COF and ZnZn-Salen-COF. b-c) PXRD patterns and refined profiles of Zn-Salen-COF and ZnZn-Salen-COF.

RESEARCH ARTICLE

Results and Discussion

The MM-Salen-COFs (M: Zn, Ni, Cu) with dual metallosalen sites were synthesized by acid-catalyzed Schiff base reaction of (1R,2R)-(-)-1,2-diaminocyclohexane and 5,5',5''-(1,3,5-triazine-2,4,6-triyl)tris(2-hydroxyisophthalaldehyde) (THFB) as well as the simultaneous metal coordination by *in situ* adding $M(\text{ClO}_4)_2 \cdot 6\text{H}_2\text{O}$ (M: Zn, Ni, Cu) via one-step solvothermal synthesis in mesitylene/ethanol solution at 120 °C for three days. The M-Salen-COF with single metallosalen site was synthesized by similar method with 1,3,5-triazine-2,4,6-tris(4'-hydroxy-5'-formylphenyl)benzene (THFB) as reactant (Figures 1a and S1).^[12b] The crystalline structure of Zn-Salen-COF and ZnZn-Salen-COF were determined by powder X-ray diffraction (PXRD) analysis. As shown in Figures 1b and 1c, the PXRD patterns show that the Zn-Salen-COF and ZnZn-Salen-COF display sharp PXRD diffraction peaks in the range of low degree, indicating the long-range order in the framework. However, no obvious PXRD diffraction peaks can be observed in these COFs without *in situ* introducing metal ions (Figure S2), indicating the necessary of introducing metal ions for the formation of crystalline structure. The possible extension structures of these two Salen-COFs were further built by the Materials Studio program and the results show that both Zn-Salen-COF and ZnZn-Salen-COF tend to stagger AA stacking model (corresponding AB stacking model and PXRD were shown in Figures S3-S4). Figures 1b and 1c show that the PXRD diffraction peaks of Zn-Salen-COF at 3.54, 7.19, 9.46, and 25.37° corresponding to (100), (200), (210) and (001) planes of *P*321 space group, respectively, and the peaks of ZnZn-Salen-COF at 3.51, 7.32, and 26.57° corresponding to (100), (200) and (001) planes of *P*321 space group, respectively. The Pawley refined profiles of these Salen-COFs match well with the PXRD patterns observed by experiments, resulting in good consistency factors ($R_{\text{wp}} = 4.06\%$ and $R_p = 5.07\%$ for Zn-Salen-COF; $R_{\text{wp}} = 5.24\%$ and $R_p = 4.02\%$ for ZnZn-Salen-COF) and reasonable profile differences. Furthermore, the unit-cell parameters of these Salen-COFs were optimized by a universal force field (Zn-Salen-COF: $a = 28.80 \text{ \AA}$, $b = 28.80 \text{ \AA}$, $c = 3.50 \text{ \AA}$, $\alpha = 90^\circ$, $\beta = 90^\circ$, $\gamma = 120^\circ$; ZnZn-Salen-COF: $a = 27.86 \text{ \AA}$, $b = 27.86 \text{ \AA}$, $c = 6.60 \text{ \AA}$, $\alpha = 90^\circ$, $\beta = 90^\circ$, $\gamma = 120^\circ$). The PXRD diffraction peaks observed at 25.31° for Zn-Salen-COF and 26.57° for ZnZn-Salen-COF correspond to their interlayer distances, with the calculated *d*-spacing values of 3.51 and 3.34 Å, respectively (Figure 1a).

The chemical structures of the Zn-Salen-COF and ZnZn-Salen-COF were confirmed through Fourier transform infrared (FT-IR) spectroscopy and ^{13}C cross-polarization magic angle spinning solid-state nuclear magnetic resonance (CP/MAS ssNMR). As shown in Figures 2a and S5, the FT-IR spectra exhibited typical imine bond ($-\text{C}=\text{N}-$) stretching vibration bands at 1639 cm^{-1} for Zn-Salen-COF and 1638 cm^{-1} for ZnZn-Salen-COF, accompanied by the absence of the $-\text{C}=\text{O}$ stretching vibration peak. Additionally, the CP/MAS ssNMR spectra displayed characteristic carbon signals in the range of 158–170 ppm (Figure 2b), further validating the presence of $-\text{C}=\text{N}-$ in ZnZn-Salen-COF. In addition, the chemical shift signals around 65 ppm in the CP/MAS ssNMR indicated the presence of C–N bond from diaminocyclohexane. These above findings

conclusively support the successful synthesis of Zn-Salen-COF and ZnZn-Salen-COF. The porosity of these materials was further determined by N_2 adsorption–desorption isotherms at 77 K (Figures 2c and S6). The results show that the both Zn-Salen-COF and ZnZn-Salen-COF exhibited type I feature, revealing that both of them possessed micropore structure. The calculated value of Brunauer–Emmett–Teller (BET) surface areas of Zn-Salen-COF and ZnZn-Salen-COF are 608.45 and 273.20 $\text{m}^2 \text{g}^{-1}$, the corresponding pore sizes are 2.00 and 1.37 nm, respectively.

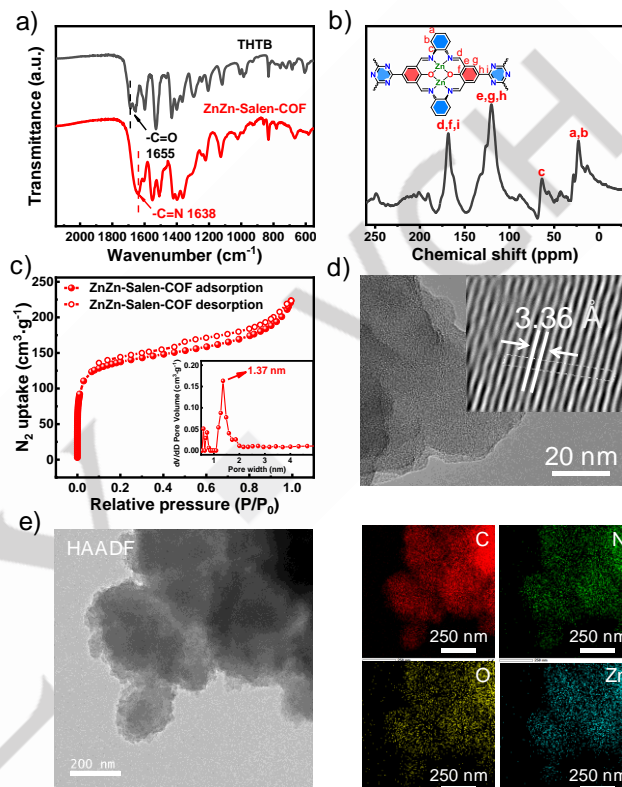


Figure 2. The characterizations of ZnZn-Salen-COF. a) FT-IR spectra for THFB and ZnZn-Salen-COF. b) ^{13}C CP/MAS ssNMR of ZnZn-Salen-COF. c) N_2 adsorption–desorption isotherms and pore size distribution profiles (insert) for ZnZn-Salen-COF. d) HR-TEM image and lattice fringes (insert) of ZnZn-Salen-COF. e) HAADF-TEM elemental mapping of ZnZn-Salen-COF.

The scanning electron microscopy (SEM) images of Zn-Salen-COF and ZnZn-Salen-COF show an aggregation particle morphology, and the EDS elements mapping show the elements of C, N, O, Zn are evenly distributed in Zn-Salen-COF and ZnZn-Salen-COF, with contents of Zn are 4.24 and 10.52 wt%, respectively (Figures S7-S8). The accurate metal contents in these materials were further tested by inductively coupled plasma-optical emission spectrometry (ICP-OES). The results show that the content of Zn is 6.44 wt% for Zn-Salen-COF and 13.07 wt% for ZnZn-Salen-COF (Table S3), which are consistent with their theoretical values. Figures 2d and S9-S10 show that the high-resolution transmission electron microscopy (HR-TEM) image of Zn-Salen-COF and ZnZn-Salen-COF display obvious lattice fringes with the lattice spacing of 3.47 and 3.36 Å, respectively, which are consistent with their interlayer distances from crystal structure. Moreover, elemental mapping in HAADF-

RESEARCH ARTICLE

TEM mode shows that the elements of C, N, O, Zn are uniformly distributed in ZnZn-Salen-COF (Figure 2e). The thermogravimetric analysis (TGA) curve shows that Zn-Salen-COF and ZnZn-Salen-COF can maintain structure stability up to 300°C in air atmosphere (Figure S11). Moreover, the chemical stability of ZnZn-Salen-COF was determined by immersing the

sample in various solutions including DMSO, DMF, ethanol, THF, acetone, boiling water, acid and base solutions of pH from 1 to 14 for seven days. The identical PXRD diffraction patterns before and after immersing indicate its notable chemical stability even in 1 M NaOH, and 2 M HCl solutions. (Figure S12).

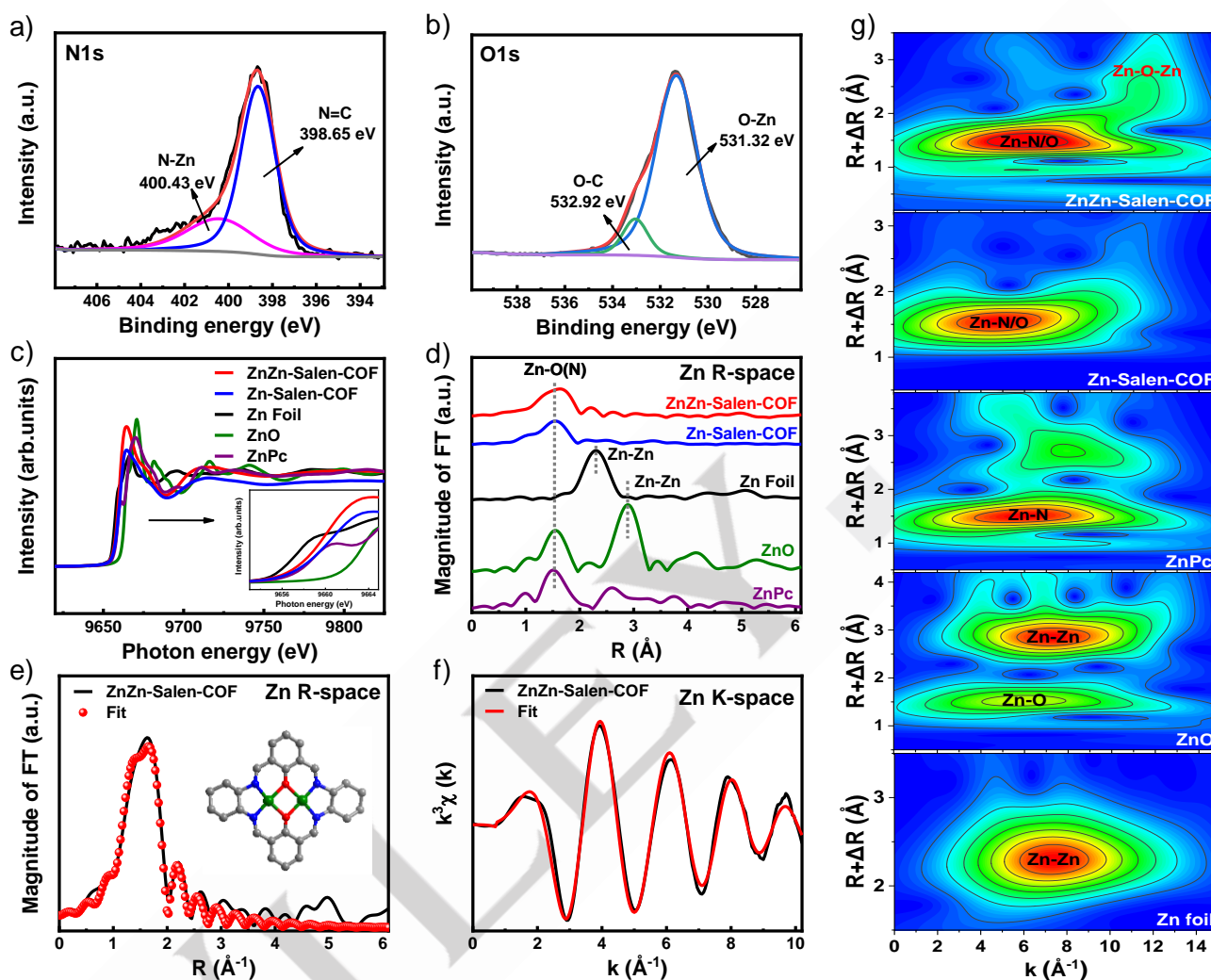


Figure 3. XPS and X-ray absorption spectroscopy analysis. a-b) HR-XPS of N 1s and O 1s spectra for ZnZn-Salen-COF. c-d) XANES and FT-EXAFS spectra of ZnZn-Salen-COF, Zn-Salen-COF, Zn Foil, ZnO, and ZnPc, respectively. e-f) EXAFS fitting results of ZnZn-Salen-COF at R-space and K-space, respectively. g) Wavelet transform of ZnZn-Salen-COF, Zn-Salen-COF, ZnPc, ZnO and Zn foil, respectively.

To study electronic properties and local coordination structures in these Salen-COFs, X-ray photoelectron spectroscopy (XPS) was conducted. The high-resolution (HR) XPS of Zn 2p spectrum for ZnZn-Salen-COF displays two distinct binding energy peaks at 1044.52 and 1021.52 eV from Zn 2p_{1/2} and Zn 2p_{3/2}, respectively, indicating that element of Zn exists in ZnZn-Salen-COF (Figure S13). The HR-XPS spectrum of O 1s shows that the binding energy peak at 531.32 eV corresponds to the O-Zn bond. And in the HR-XPS spectrum of N 1s, the binding energy peak of N-Zn bond at 400.43 eV can be observed (Figures 3a-3b). Above results indicate the existence of Zn-N and Zn-O coordination modes in ZnZn-Salen-COF. Similarly, the same

coordination modes were observed in HR-XPS spectra (N 1s, O 1s and Zn 2p) of Zn-Salen-COF (Figure S14). In addition, the XPS results of the other two dual metallosalen COFs also indicate the presence of Ni-N, Ni-O and Cu-N, Cu-O coordination modes in their respective COFs structures, further confirming the metal coordination environment (Figures S15-S16).

The X-ray absorption near edge structure (XANES) spectra in Figure 3c show that the Zn K-edge of ZnZn-Salen-COF and Zn-Salen-COF was between those of Zn foil and ZnO, indicating that the oxidation states of Zn are 0 ~ +2. Subsequently, Figure 3d shows that the Fourier transform (FT) extended X-ray absorption fine structure (EXAFS) spectra of the Zn K-edge for both ZnZn-

RESEARCH ARTICLE

Salen-COF and Zn-Salen-COF appeared a main peak at 1.49 Å, which located on the scattering paths of Zn–N in ZnPc and Zn–O bonds in ZnO, indicating that Zn atoms in these systems were coordinated by both N and O atoms. No signal of Zn–Zn bond was observed in the ZnZn-Salen-COF and Zn-Salen-COF, thus validating the absence of Zn nanoparticles or clusters. The coordination number and structure of the Zn centers were determined by fitting the first shell in EXAFS analysis. By integrating the *K*-space results of Zn-Salen-COF and ZnZn-Salen-COF fitting, it can be deduced that Zn adopts a Zn–N₂O₂ coordination configuration, with the average bond lengths of ~2.03 Å for Zn–O bonds and ~1.94 Å for Zn–N bonds (Figures 3e–3f, S17–S18 and Table S4). Wavelet transform (WT) further visualized the metal species' coordination forms. Figure 2g show that the maximum intensity of Zn–O, Zn–Zn, and Zn–N bonds in

ZnO and ZnPc are 5.95, 7.21, and 6.03 Å^{−1}. For the WT of Zn-Salen-COF, the maximum intensity appeared at 5.75 Å^{−1}, which is attributed to the Zn–O bond and Zn–N. As for ZnZn-Salen-COF, there are two apparent shells in 6.04 and 10.25 Å^{−1}, which could be assigned to Zn–O (N) and Zn–O–Zn bonds. All the above analyses clearly indicate the stable Zn–N₂O₂ coordination mode of Zn ions in the Salen unit of Zn-Salen-COF and ZnZn-Salen-COF. Similarly, the XANES and EXAFS of other two dual metallosalen COFs were tested, as presented in the Figures S19–S22. The results indicate that Ni and Cu exhibit Ni–N₂O₂ and Cu–N₂O₂ coordination configurations in NiNi-Salen-COF and CuCu-Salen-COF, respectively (Tables S5–S6). These findings are consistent with the coordination environment observed in ZnZn-Salen-COF.

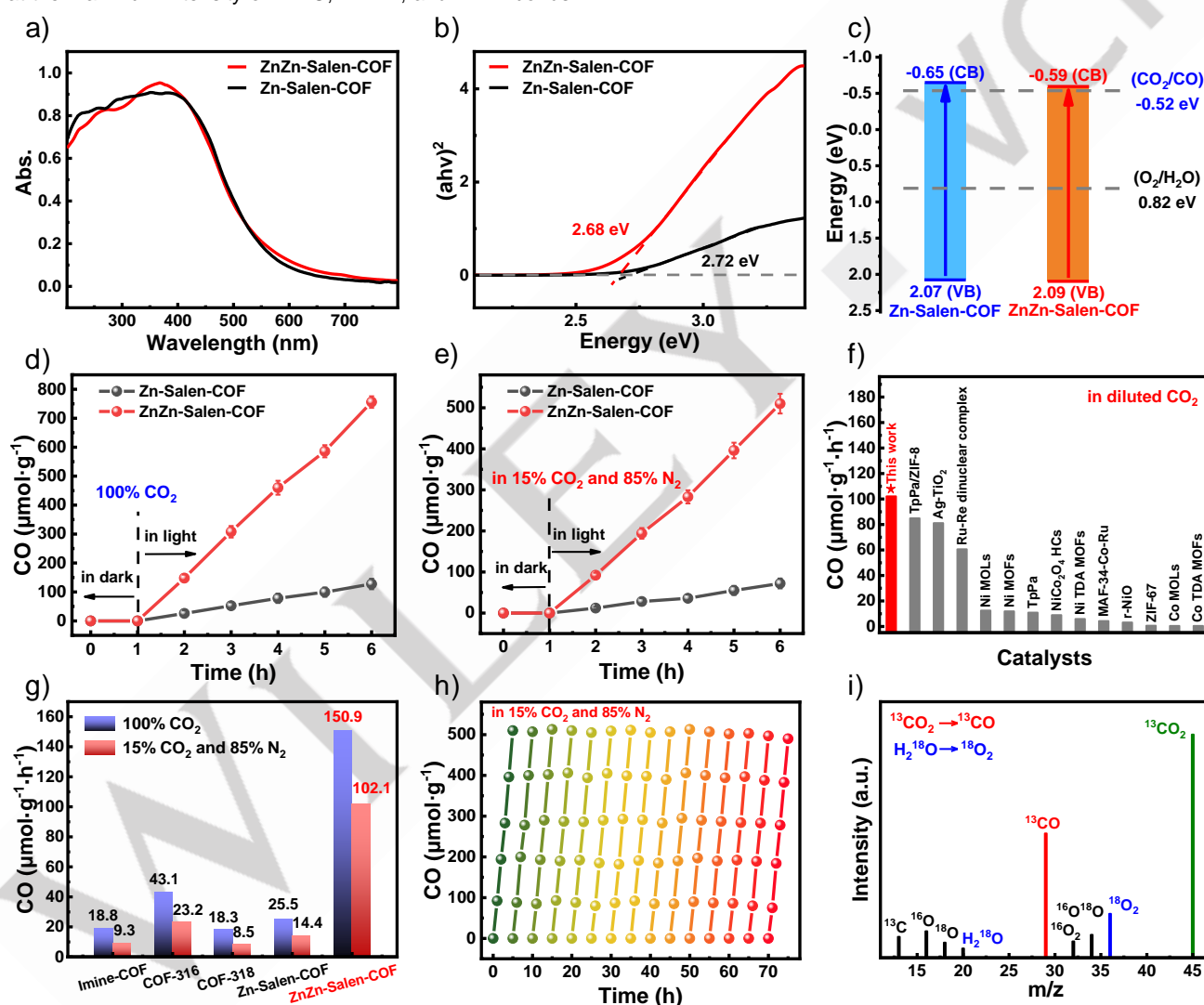


Figure 4. a–c) UV–vis DRS spectra, optical bandgap and energy band structures for ZnZn-Salen-COF and Zn-Salen-COF. d) Time-yield plots of performance of photocatalytic CO₂ reduction to CO. e) Performance of photocatalytic CO₂ reduction to CO with diluted CO₂ (15% CO₂ and 85% N₂). f) Comparison of the performances of CO production rate with reported MOFs or COFs-based photocatalysts in diluted CO₂ atmosphere. g) Performance of photocatalytic CO₂ reduction for various photocatalysts. h) Photocatalytic CO₂RR cycle stability for ZnZn-Salen-COF. i) Mass spectrometry for CO₂RR and H₂O oxidation at ¹³CO₂ and H₂¹⁸O atmosphere.

RESEARCH ARTICLE

The UV-Vis diffuse reflectance spectroscopy (DRS) and Mott-Schottky (M-S) analyses were conducted to determine their band structure. Figure 4a illustrates strong light absorption within the 380–550 nm range for both Zn-Salen-COF and ZnZn-Salen-COF, with calculated band gaps of 2.72 and 2.68 eV (Figure 4b), respectively, through Tauc plots from the corresponding DRS. The flat band potentials of Zn-Salen-COF and ZnZn-Salen-COF were determined to be -0.74 and -0.68 V relative to the saturated calomel electrode (SCE) by M-S test (Figures S23–S24). Consequently, the conduction band (CB) potentials of Zn-Salen-COF and ZnZn-Salen-COF were estimated at -0.65 and -0.59 V, respectively (relative to the normal hydrogen electrode (NHE) at pH = 7). Combining the obtained band gaps and CB positions, the valence band (VB) positions of Zn-Salen-COF and ZnZn-Salen-COF were calculated to be 2.07 and 2.09 V, respectively. Based on the above results, it is evident that both of the M-COFs are thermodynamically suitable for CO₂ conversion to CO (-0.52 V vs NHE, pH = 7) and simultaneous water oxidation to O₂ (0.82 V vs NHE, pH = 7), as depicted in Figure 4c.

Based on the above discussion, artificial photosynthetic CO₂ reduction activities of Zn-Salen-COF and ZnZn-Salen-COF were further conducted in CH₃CN/H₂O system under simulated visible light (420 ≤ λ ≤ 800 nm) without any additional agents. Figure 4d shows that single metal Zn-Salen-COF only shows a low CO₂ conversion to CO activity of 25.5 μmol g⁻¹ h⁻¹, while dual metal ZnZn-Salen-COF displays an obviously enhanced CO₂-to-CO conversion activity of 150.9 μmol g⁻¹ h⁻¹, which is ~6 times higher than single metal Zn-Salen-COF. Moreover, artificial photosynthetic diluted CO₂ reduction activity was conducted in simulated flue gases conditions (15% CO₂ atmosphere). As shown in Figure 4e, the dual metal ZnZn-Salen-COF still maintains a high CO₂-to-CO conversion activity of 102.1 μmol g⁻¹ h⁻¹ in diluted CO₂ conditions, which is significantly higher than that of single metal Zn-Salen-COF (14.4 μmol g⁻¹ h⁻¹). Notably, the photocatalytic activity ZnZn-Salen-COF in diluted CO₂ atmosphere is the highest among various reported photocatalysts under similar conditions (Figure 4f and Table S7), even outperforming the activities of most COF-based photocatalysts under high concentration CO₂ atmosphere (Table S8).^[17] To give a more convective comparison, some typical COFs (including COF-316, COF-318 and Imine-COF) with artificial photosynthetic activity were synthesized and their photocatalytic performances were determined (PXRD see Figures S25–S27).^[18] Obviously, the dual metal ZnZn-Salen-COF shows the highest CO₂RR activity compared to the above COFs (Figure 4g), illustrating the advantage of ZnZn-Salen-COF in CO₂RR. In addition, different dual metallosalen MM-Salen-COFs (M: Ni, Cu) were further synthesized (PXRD see Figure S28), and the results of photocatalytic measurements show that the ZnZn-Salen-COF shows the highest photocatalytic CO₂RR activity (Figure S29). Moreover, only trace H₂ and HCOO⁻ products for ZnZn-Salen-COF photocatalyst were detected in GC, IC and NMR (Figures S30–S32), which indicated that high CO₂RR selectivity (>99%) could still be maintained in a low concentration CO₂ atmosphere.

Additionally, the apparent quantum efficiency (AQE) of ZnZn-Salen-COF during the CO₂RR process was assessed across various wavelengths. The highest AQE value of 1.9% was

recorded at 420 nm, after which the AQE declined with the increase of the wavelength of incident light, and this trend aligns with the light absorption characteristics inherent to ZnZn-Salen-COF (Figure S33). Notably, the ZnZn-Salen-COF shows excellent artificial photosynthetic diluted CO₂RR stability in the reused 15 consecutive cycles in 75 h (Figure 4h). Finally, the photocatalytic test with ¹³CO₂ as the gas source and H₂¹⁸O as electron donor was carried out to determine the sources of produced CO and O₂. The gas products were monitored by mass spectrometer and the peak from ¹³CO (m/z = 29) and ¹⁸O₂ (m/z = 36) can be detected, which confirm that the produced CO and O₂ are exclusively derived from the reduction of CO₂ and H₂O oxidation reaction (Figure 4i). To confirm the structural integrity of ZnZn-Salen-COF in photocatalytic process, PXRD, FT-IR, XPS, TEM and mapping measurements were carried out for the sample after CO₂RR. No obvious change can be observed in these characterizations for ZnZn-Salen-COF before and after reaction, demonstrating its structural and morphological stability (Figures S34–S37).

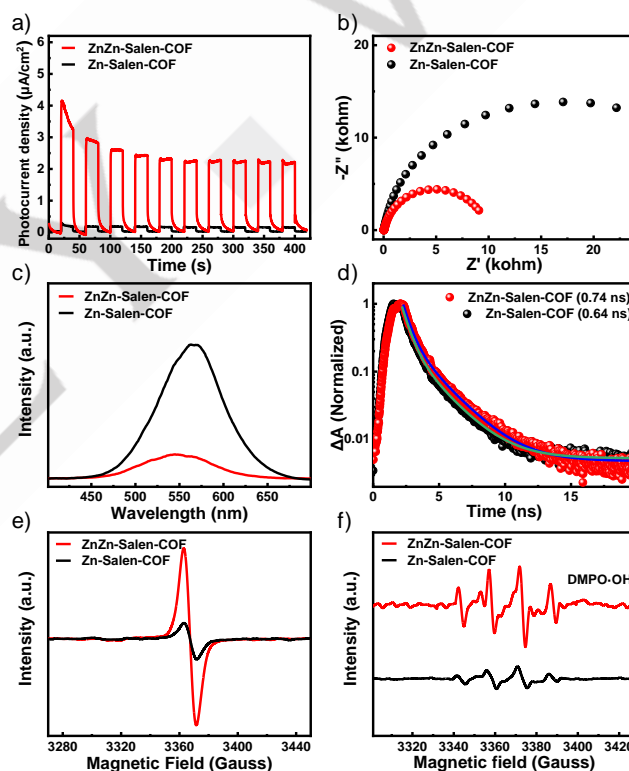


Figure 5. a) Transient photocurrent responses, b) EIS curves, c) PL spectra, d) Time-resolved PL spectra, e) EPR spectra under 420 nm light irradiation, and f) EPR spectra of DMPO-OH adducts in aqueous solution for ZnZn-Salen-COF and Zn-Salen-COF.

To investigate the dynamic behavior of photogenerated charge carriers, electrochemical impedance spectroscopy (EIS), transient photocurrent responses, photoluminescence (PL) with PL lifetimes, and electron paramagnetic resonance (EPR) were conducted. Figure 5a shows that dual metal ZnZn-Salen-COF shows a largely stronger photocurrent resonance compared to single metal Zn-Salen-COF. The EIS results show the radius of

RESEARCH ARTICLE

the Nyquist curve of ZnZn-Salen-COF is smaller than that of Zn-Salen-COF, indicating a smaller charge transfer resistance in ZnZn-Salen-COF (Figure 5b). In addition, ZnZn-Salen-COF exhibits more obvious fluorescence quench and longer PL lifetime compared to Zn-Salen-COF (Figures 5c-5d). The above results illustrate that dual metal ZnZn-Salen-COF shows high electron-hole separation efficiency and fast charge transfer ability compared with single metal Zn-Salen-COF. The room temperature EPR spectra show that the ZnZn-Salen-COF displays an apparently stronger EPR signal than single metal Zn-Salen-COF (Figure 5e), indicating stronger electron delocalization existed in the dual metal ZnZn-Salen-COF. Moreover, the EPR spectra of hydroxyl ($\cdot\text{OH}$) radicals via 5, 5-dimethyl-1-pyrroline N-oxide (DMPO) were measured for ZnZn-Salen-COF and Zn-Salen-COF. The results show that the DMPO- $\cdot\text{OH}$ signal of dual metal ZnZn-Salen-COF is obviously stronger than that of single metal Zn-Salen-COF under light irradiation (Figure 5f), suggesting the ZnZn-Salen-COF is more feasible to drive the oxidation reaction of $\cdot\text{OH}$ to O_2 .

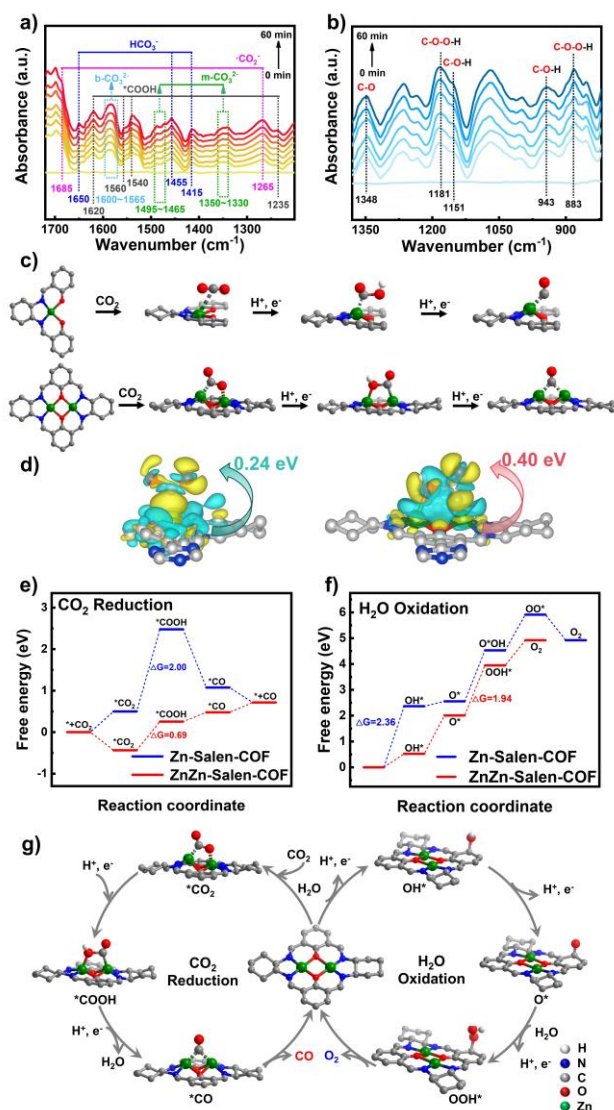


Figure 6. a-b) *In situ* DRIFTS of ZnZn-Salen-COF for CO_2 reduction and water oxidation in the dark (background) and under visible-light irradiation (irradiation

time 0-60 min). c) The adsorption intermediates of single/dual metallosalen COFs for artificial photosynthetic CO_2 reduction. d) The Bader charge for Zn-Salen-COF-COOH (left) and ZnZn-Salen-COF-COOH (right). e) Free energy profiles of ZnZn-Salen-COF and Zn-Salen-COF in the CO_2 reduction process. f) Free energy profiles of ZnZn-Salen-COF and Zn-Salen-COF in the H_2O oxidation process. g) Schematic diagram of proposed artificial photosynthetic CO_2 reduction mechanism for ZnZn-Salen-COF.

The *in situ* diffuse reflectance infrared Fourier transform spectra (DRIFTS) measurement was carried out for ZnZn-Salen-COF to detect the reaction intermediates in the artificial photosynthetic CO_2 RR process under CO_2 and water vapor conditions with various irradiation time. Figure 6a shows that various CO_2 RR intermediate species including CO_2 adsorption ($^*\text{CO}_2$ at 1265 and 1685 cm^{-1}) bidentate carbonate ($\text{b-}^*\text{CO}_3^{2-}$ at 1565 cm^{-1}), monodentate carbonate ($\text{m-}^*\text{CO}_3^{2-}$ at 1488, 1473 and 1350–1330 cm^{-1}), and bicarbonate (HCO_3^- at 1650, 1455 and 1415 cm^{-1}) were detected and the characteristic peak intensity gradually increased with the reaction time in DRIFTS. Furthermore, the characteristic peaks at 1235 and 1620 cm^{-1} in the *in situ* DRIFTS spectra can be attributed to $^*\text{COOH}$ intermediate, and gradually strengthened over visible-light irradiation time (Figure S38), which is regarded as the key reaction intermediate in the artificial photosynthesis of CO_2 to CO .^[19] However, there are no obvious $^*\text{COOH}$ characteristic peaks in the DRIFTS spectrum of Zn-Salen-COF, which is consistent with its lower photocatalytic CO_2 reduction activity compared with dual metal ZnZn-Salen-COF (Figure S39). Meanwhile, the water oxidation process was analyzed through *in situ* DRIFTS. Figure 6b demonstrates that with prolonged illumination time in a pure water vapor atmosphere, the peaks related to C-O stretching in the key oxygen-containing intermediates, including C-O-H (1152 and 944 cm^{-1}) and C-O-O-H (1180 and 882 cm^{-1}) intensified progressively. The identification of these oxygen-containing intermediates serves as evidence for the taking place of the H_2O oxidation reaction in the ZnZn-Salen-COF.

Based on the above obtained results, the density functional theory (DFT) calculations were performed to explore the artificial photosynthetic CO_2 RR mechanism in single metal Zn-Salen-COF and dual metal ZnZn-Salen-COF by evaluating the thermodynamics feasibility of CO_2 RR process. This process includes the adsorption of CO_2 molecules at the metal active site forming $^*\text{CO}_2$, followed by two-step consecutive proton-coupled electron transfer (PCET) of $^*\text{CO}_2$ to sequentially form $^*\text{COOH}$ and $^*\text{CO}$ intermediates, then $^*\text{CO}$ desorption to produce CO . Here, two difference adsorption modes in single and dual metal Salen-COFs were considered, including single metal site adsorption of CO_2 molecules, as well as dual metal sites co-adsorption and activation of CO_2 molecules. As illustrated in Figure 6c, the single metal Zn-Salen-COF adsorbs CO_2 through the interaction between the metal and the carbon atom of CO_2 molecule. In contrast, the neighboring dual metal sites in ZnZn-Salen-COF facilitate the co-adsorption and activation of CO_2 molecules through simultaneous interactions between both metal sites and the carbon and oxygen atoms of the CO_2 molecule. Additionally, the charge difference density analysis indicates that the Bader

RESEARCH ARTICLE

charge of ZnZn-Salen-COF-COOH (0.40 eV) is higher than Zn-Salen-COF-COOH (0.24 eV), suggesting a stronger adsorption of $^*\text{COOH}$ intermediate on dual metal ZnZn-Salen-COF compared to the single metal Zn-Salen-COF (Figure 6d). Furthermore, the ZnZn-Salen-COF with dual metal synergistic effect exhibits a lower rate-determining step (RDS) energy barrier (ΔG_{COOH}^*) of 0.69 eV than single metal Zn-Salen-COF of 2.00 eV, indicating that dual metal ZnZn-Salen-COF is more beneficial for photoreduction CO_2 to CO product (Figure 6e). Therefore, from a thermodynamic perspective, dual metal ZnZn-Salen-COF demonstrates greater potential for photocatalytic conversion CO_2 to CO compared to the single metal Zn-Salen-COF, owing to the synergistic effect of the neighboring dual metal sites within the ZnZn-Salen-COF structure.

Additionally, the CO_2 adsorption isotherms indicate that the low concentration CO_2 adsorption capacity of dual metal ZnZn-Salen-COF (0.58 mmol g^{-1}) is 3.5 times higher than that of the single metal Zn-Salen-COF (0.18 mmol g^{-1}) at a relative pressure (P/P_0) of 0.15 and a temperature of 298 K (Figure S40). This result demonstrates that the dual metal ZnZn-Salen-COF exhibits superior CO_2 adsorption capacity due to the synergistic adsorption effect of dual metal sites, which enhances the adsorption of CO_2 molecules at low relative pressures, thereby improving the photocatalytic performance for diluted CO_2 reduction. Moreover, the water oxidation path was calculated by our previous reported work.^[12b] The energy barriers associated with the rate-determining steps for water oxidation in single and dual metal Salen-COFs are presented. As illustrated in Figure 6f, the RDS free energy barrier for the formation of OOH^* (1.94 eV) in the dual metal ZnZn-Salen-COF is significantly lower than that for the formation of OH^* (2.36 eV) in the single metal Zn-Salen-COF. In addition, the water oxidation process in ZnZn-Salen-COF can directly produce O_2 without going through the intermediate state of OO^* , indicating that the incorporation of dual metal sites in ZnZn-Salen-COF effectively facilitates the oxidation of H_2O during the photocatalytic process. Finally, the artificial photosynthetic CO_2 reduction and water oxidation pathways of ZnZn-Salen-COF are shown in Figure 6g.

Conclusion

In summary, a series of dual-metal sites Salen-based COFs featuring different metal sites were synthesized via a one-step solvothermal strategy. These obtained dual-metallosalen COFs exhibit impressive performance in artificial photosynthetic CO_2 reduction. Particularly, the dual-metal ZnZn-Salen-COF demonstrates a prominent visible-light-driven CO_2 -to-CO conversion rate of $150.9 \mu\text{mol g}^{-1} \text{ h}^{-1}$, which is ~ 6 times higher than the single metal Zn-Salen-COF. Notably, the dual-metal ZnZn-Salen-COF displays a remarkable diluted CO_2 conversion activity of $102.1 \mu\text{mol g}^{-1} \text{ h}^{-1}$ under a diluted CO_2 (15%) atmosphere, which is significantly higher than that of Zn-Salen-COF with single metal site ($14.4 \mu\text{mol g}^{-1} \text{ h}^{-1}$). It is a record high activity among COFs- and MOFs-based photocatalysts for artificial photosynthetic diluted CO_2 reduction under the same reaction conditions. Further investigations and theoretical calculations suggest that the synergistic effect between the

neighboring dual-metal sites in the ZnZn-Salen-COF facilitates low concentration CO_2 adsorption and activation, thereby lowering the energy barrier of the rate-determining step and maintaining the high CO_2 RR activity in diluted CO_2 atmosphere. This work provides a new strategy of constructing synergistic dual metal sites in M-COFs for artificial photosynthetic diluted CO_2 reduction.

Supplemental Information includes 40 Figures and 8 Tables.

Acknowledgements

This work was financially supported by the National Natural Science Foundation of China (No.22178077, 22102178), Shandong Provincial Natural Science Foundation (No. ZR2022MB126), Postdoctoral Scientific Research Star-up Project in Heilongjiang Province, Fundamental Research Foundation for Universities of Heilongjiang Province and Key Laboratory of Functional Inorganic Material Chemistry (Heilongjiang University), Ministry of Education.

Conflict of Interest

The authors declare no conflict of interest.

Keywords: Dual metallosalen • Covalent organic framework • Artificial photosynthesis • Diluted CO_2 reduction

References

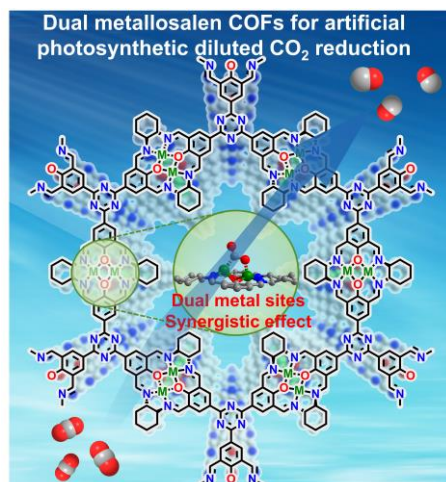
- [1] a) Q. Wang, S. Kalathil, C. Pornrungraj, C. D. Sahm, E. Reisner, *Nat. Catal.* **2022**, *5*, 633-641; b) M. Mathis, F. Lacroix, S. Hagemann, D. M. Nielsen, T. Ilyina, C. Schrum, *Nat. Clim. Change* **2024**, *14*, 373-379; c) L. X. Wang, B. C. Zhu, J. J. Zhang, J. B. Ghasemi, M. Mousavi, J. G. Yu, *Matter* **2022**, *5*, 4187-4211.
- [2] a) P. Saha, S. Amanullah, A. Dey, *Acc. Chem. Res.* **2022**, *55*, 134-144; b) S. Fang, M. Rahaman, J. Bharti, E. Reisner, M. Robert, G. A. Ozin, Y. H. Hu, *Nat. Rev. Methods Primers* **2023**, *3*, 61; c) X. Li, J. G. Yu, M. Jaroniec, X. B. Chen, *Chem. Rev.* **2019**, *119*, 3962-4179; d) S. Kreft, R. Schoch, J. Schneidewind, J. Rabeah, E. V. Kondratenko, V. A. Kondratenko, H. Junge, M. Bauer, S. Wohlrab, M. Beller, *Chem* **2019**, *5*, 2276-2276.
- [3] a) J. L. Yu, L. B. Huang, Q. X. Tang, S. B. Yu, Q. Y. Qi, J. S. Zhang, D. Y. Ma, Y. F. Lei, J. J. Su, Y. Song, J. C. Eloi, R. L. Harniman, U. Borucu, L. Zhang, M. H. Zhu, F. Tian, L. L. Du, D. L. Phillips, I. Mannes, R. Q. Ye, J. Tian, *Nat. Catal.* **2023**, *6*, 464-475; b) F. Kuttassery, Y. Ohsaki, A. Thomas, R. Kamata, Y. Ebato, H. Kumagai, R. Nakazato, A. Sebastian, S. Mathew, H. Tachibana, O. Ishitani, H. Inoue, *Angew. Chem., Int. Ed.* **2023**, *62*, e202308956; c) H. W. Zhang, J. T. Ming, J. W. Zhao, Q. Gu, C. Xu, Z. X. Ding, R. S. Yuan, Z. Z. Zhang, H. X. Lin, X. X. Wang, J. L. Long, *Angew. Chem., Int. Ed.* **2019**, *58*, 7718-7722.
- [4] a) L. Z. Liu, S. B. Wang, H. W. Huang, Y. H. Zhang, T. Y. Ma, *Nano Energy* **2020**, *75*, 104959; b) J. R. Ran, M. Jaroniec, S. Z. Qiao, *Adv. Mater.* **2018**, *30*, 1704649; c) Z. W. Chen, H. Zhang, P. J. Guo, J. J. Zhang, G. Tira, Y. J. Kim, Y. M. A. Wu, Y. Z. Liu, J. G. Wen, T. Rajh, J. Niklas, O. G. Poluektov, P. D. Laible, E. A. Rozhkova, *J. Am. Chem. Soc.* **2019**, *141*, 11811-11815; d) H. Jung, C. Kim, H. W. Yoo, J. You, J. S. Kim, A. Jamal, I. Gereige, J. W. Ager, H. T. Jung, *Energy Environ. Sci.* **2023**, *16*, 2869-2878.
- [5] a) K. Geng, T. He, R. Liu, K. T. Tan, Z. Li, S. Tao, Y. Gong, Q. Jiang, D. Jiang, *Chem. Rev.* **2020**, *120*, 8814-8933; b) X. Feng, X. S. Ding, D. L. Jiang, *Chem. Soc. Rev.* **2012**, *41*, 6010-6022; c) W. Han, W. Hui, W. Ziwei, T. Lin, Z. Guangming, X. Piao, C. Ming, X. Ting, Z. Chengyun, L.

RESEARCH ARTICLE

- Xi, H. Danlian, Z. Yuan, W. Zixuan, T. Junwang, *Chem. Soc. Rev.* **2020**, *49*, 4135-4165; d) X. Han, C. Yuan, B. Hou, L. J. Liu, H. Y. Li, Y. Liu, Y. Cui, *Chem. Soc. Rev.* **2020**, *49*, 6248-6272; e) S. M. J. Rogge, A. V. Bavykina, J. Hajek, H. Garcia, A. I. Olivossuarez, A. Sepulvedaescribano, A. Vimont, G. Clet, P. Bazin, F. Kapteijn, *Chem. Soc. Rev.* **2017**, *46*, 3134-3184; f) Y. S. Wei, M. Zhang, R. Q. Zou, Q. Xu, *Chem. Rev.* **2020**, *120*, 12089-12174.
- [6] a) A. P. Côté, A. I. Benin, N. W. Ockwig, M. O'Keeffe, A. J. Matzger, O. M. Yaghi, *Science* **2005**, *310*, 1166-1170; b) Q. Guan, L. L. Zhou, Y. B. Dong, *Chem. Soc. Rev.* **2022**, *51*, 6307-6416; c) X. Y. Guan, Q. R. Fang, Y. S. Yan, S. L. Qiu, *Acc. Chem. Res.* **2022**, *55*, 1912-1927.
- [7] a) J. Q. Dong, X. Han, Y. Liu, H. Y. Li, Y. Cui, *Angew. Chem., Int. Ed.* **2020**, *59*, 13722-13733; b) L. A. Baldwin, J. W. Crowe, D. A. Pyles, P. L. McGrier, *J. Am. Chem. Soc.* **2016**, *138*, 15134-15137; c) W. K. Han, Y. Liu, X. D. Yan, Z. G. Gu, *Mater. Chem. Front.* **2023**, *7*, 2995-3010; d) S. Suleman, Y. Zhang, Y. Y. Qian, J. W. Zhang, Z. Y. Lin, O. Metin, Z. Meng, H. L. Jiang, *Angew. Chem., Int. Ed.* **2024**, *63*, e202314988.
- [8] a) W. Lin, F. Lin, J. Lin, Z. Xiao, D. Yuan, Y. Wang, *J. Am. Chem. Soc.* **2024**, *146*, 16229-16236; b) Y. Wang, H. He, Y. Li, W. Wang, L. Deng, L. Wu, Y. Zhang, J. Huang, P. Zhang, G. Yu, Y.-N. Liu, *Matter* **2024**, *10.1016/j.matt.2024.05.003*; c) B. B. Rath, S. Krause, B. V. Lotsch, *Adv. Funct. Mater.* **2023**, 2309060; d) T. Luo, L. Gilmanova, S. Kaskel, *Coord. Chem. Rev.* **2023**, *490*, 215210; e) S. Gao, Q. Zhang, X. Su, X. Wu, X.-G. Zhang, Y. Guo, Z. Li, J. Wei, H. Wang, S. Zhang, J. Wang, *J. Am. Chem. Soc.* **2023**, *145*, 9520-9529.
- [9] a) M.-H. Li, C. Xu, Y.-W. Yang, *Coord. Chem. Rev.* **2024**, *512*, 215894; b) X. Han, Q. C. Xia, J. J. Huang, Y. Liu, C. X. Tan, Y. Cui, *J. Am. Chem. Soc.* **2017**, *139*, 8693-8697; c) L. H. Li, X. L. Feng, X. H. Cui, Y. X. Ma, S. Y. Ding, W. Wang, *J. Am. Chem. Soc.* **2017**, *139*, 6042-6045; d) L. S. Sun, M. Lu, Z. F. Yang, Z. Y. Yu, X. Su, Y. Q. Lan, L. Chen, *Angew. Chem., Int. Ed.* **2022**, *61*, e202204326; e) M. Lu, J. Liu, Q. Li, M. Zhang, M. Liu, J. L. Wang, D. Q. Yuan, Y. Q. Lan, *Angew. Chem., Int. Ed.* **2019**, *58*, 12392-12397; f) Y. Z. Zhang, L. L. Cao, G. Y. Bai, X. W. Lan, *Small* **2023**, *19*, 2300035.
- [10] a) Y. H. Kim, J. P. Jeon, Y. Kim, H. J. Noh, J. M. Seo, J. Kim, G. Lee, J. B. Baek, *Angew. Chem., Int. Ed.* **2023**, *62*, e202307991; b) P. F. Dong, X. Y. Xu, R. A. Luo, S. Yuan, J. Zhou, J. P. Lei, *J. Am. Chem. Soc.* **2023**, *145*, 15473-15481; c) S. S. Zhao, J. Liang, D. H. Si, M. J. Mao, Y. B. Huang, R. Cao, *Appl. Catal., B* **2023**, *333*, 122782.
- [11] a) W. Zhou, X. Wang, W. Zhao, N. Lu, D. Cong, Z. Li, P. Han, G. Ren, L. Sun, C. Liu, W. Q. Deng, *Nat. Commun.* **2023**, *14*, 6971; b) Y. Yang, H. Y. Zhang, Y. Wang, L. H. Shao, L. Fang, H. Dong, M. Lu, L. Z. Dong, Y. Q. Lan, F. M. Zhang, *Adv. Mater.* **2023**, *35*, 2304170.
- [12] a) L. Ran, Z. W. Li, B. Ran, J. Q. Cao, Y. Zhao, T. Shao, Y. R. Song, M. K. H. Leung, L. C. Sun, J. A. Hou, *J. Am. Chem. Soc.* **2022**, *144*, 17097-17109; b) D. M. Song, W. H. Xu, J. Li, J. L. Zhao, Q. Shi, F. Li, X. Z. Sun, N. Wang, *Chin. J. Catal.* **2022**, *43*, 2425-2433; c) W. F. Zhong, R. J. Sa, L. Y. Li, Y. J. He, L. Y. Li, J. H. Bi, Z. Y. Zhuang, Y. Yu, Z. G. Zou, *J. Am. Chem. Soc.* **2019**, *141*, 7615-7621.
- [13] a) Z. C. Zhang, H. Y. Li, Y. F. Shao, L. Gan, F. Y. Kang, W. H. Duan, H. A. Hansen, J. Li, *Nat. Commun.* **2024**, *15*, 612; b) A. L. Dzubak, L. C. Lin, J. Kim, J. A. Swisher, R. Poloni, S. N. Maximoff, B. Smit, L. Gagliardi, *Nat. Chem.* **2012**, *4*, 810-816.
- [14] H. Zhong, R. J. Sa, H. W. Lv, S. L. Yang, D. Q. Yuan, X. C. Wang, R. H. Wang, *Adv. Funct. Mater.* **2020**, *30*, 2002654.
- [15] a) J. Wang, W. B. Zhu, F. Y. Meng, G. Y. Bai, Q. F. Zhang, X. W. Lan, *ACS Catal.* **2023**, *13*, 4316-4329; b) L. Zou, R. J. Sa, H. Zhong, H. W. Lv, X. C. Wang, R. H. Wang, *ACS Catal.* **2022**, *12*, 3550-3557; c) M. Zhou, Z. Q. Wang, A. H. Mei, Z. F. Yang, W. Chen, S. Y. Ou, S. Y. Wang, K. Q. Chen, P. Reiss, K. Qi, J. Y. Ma, Y. L. Liu, *Nat. Commun.* **2023**, *14*, 2473.
- [16] G. X. Yang, S. Z. Li, N. Li, P. P. Zhang, C. R. Su, L. Gong, B. T. Chen, C. Qu, D. D. Qi, T. Y. Wang, J. Z. Jiang, *Angew. Chem., Int. Ed.* **2022**, *61*, e202205585.
- [17] a) R. G. Yang, Y. M. Fu, H. N. Wang, D. P. Zhang, Z. Zhou, Y. Z. Cheng, X. Meng, Y. O. He, Z. M. Su, *Chem. Eng. J.* **2022**, *450*, 138040; b) A. P. Rangappa, D. P. Kumar, K. H. Do, J. M. Wang, Y. X. Zhang, T. K. Kim, *Adv. Sci.* **2023**, *10*, 2300073; c) Q. Li, J. N. Chang, Z. M. Wang, M. Lu, C. Guo, M. Zhang, T. Y. Yu, Y. F. Chen, S. L. Li, Y. Q. Lan, *J. Am. Chem. Soc.* **2023**, *145*, 23167-23175; d) M. Zhang, M. Lu, Z. L. Lang, J. Liu, M. Liu, J. N. Chang, L. Y. Li, L. J. Shang, M. Wang, S. L. Li, Y. Q. Lan, *Angew. Chem., Int. Ed.* **2020**, *59*, 6500-6506; e) S. Biswas, A. Dey, F. A. Rahimi, S. Barman, T. K. Maji, *ACS Catal.* **2023**, *13*, 5926-5937; f) M. Lu, M. Zhang, J. Liu, T. Y. Yu, J. N. Chang, L. J. Shang, S. L. Li, Y. Q. Lan, *J. Am. Chem. Soc.* **2022**, *144*, 1861-1871.
- [18] a) B. Zhang, M. F. Wei, H. Y. Mao, X. K. Pei, S. A. Alshimmri, J. A. Reimer, O. M. Yaghi, *J. Am. Chem. Soc.* **2018**, *140*, 12715-12719; b) C. H. Dai, T. He, L. X. Zhong, X. G. Liu, W. L. Zhen, C. Xue, S. Z. Li, D. L. Jiang, B. Liu, *Adv. Mater. Interfaces* **2021**, *8*, 2002191.
- [19] a) C. C. Chen, Q. Y. Zhang, F. T. Liu, Z. G. Zhang, Q. Liu, X. M. Fang, *J. Energy Chem.* **2024**, *92*, 282-291; b) J.-H. Zhang, H.-J. Wang, W.-J. Shi, W. Yang, J.-H. Mei, Y.-C. Wang, T.-B. Lu, D.-C. Zhong, *CCS Chem.* **2024**, *10.31635/ccschem.31024.202404351*; c) M. H. Liu, C. X. Cui, S. Yang, X. B. Yang, X. W. Li, J. He, Q. Xu, G. F. Zeng, *Angew. Chem., Int. Ed.* **2024**, *63*, e202401750.

RESEARCH ARTICLE

Entry for the Table of Contents



In this work, we constructed a series of dual metal sites dispersed Salen-based COFs (MM-Salen-COFs, M: Zn, Ni, Cu) for artificial photosynthetic diluted CO₂ reduction. The ZnZn-Salen-COF displays a remarkable CO₂ conversion activity of 102.1 $\mu\text{mol g}^{-1} \text{h}^{-1}$ under a diluted CO₂ atmosphere from simulated flue gas (15% CO₂), which is a record high activity among COF- and MOF-based photocatalysts under the same condition.